Tailoring three-dimensional interconnected nanoporous graphene micro/nano-foams for lithium-sulfur batteries

Lu, Liqiang; Pei, Fei; Abeln, Thom; Pei, Yutao T.

Published in:
Carbon

DOI:
10.1016/j.carbon.2019.10.072

Publication date:
2020

Carbon 157 (2020) 437–447

Contents lists available at ScienceDirect

Carbon

journal homepage: www.elsevier.com/locate/carbon

Tailoring three-dimensional interconnected nanoporous graphene micro/nano-foams for lithium-sulfur batteries

Liqiang Lu [a, *], Fei Pei [b], Thom Abeln [a], Yutao Pei [a]

[a] Advanced Production Engineering, Engineering and Technology Institute Groningen, University of Groningen, Nijenborgh 4, 9747, AG, Groningen, the Netherlands

[b] Department of Chemistry, James Franck Institute and Institute for Biophysical Dynamics, The University of Chicago, 5801 S Ellis Ave, Chicago, IL, 60637, USA

ARTICLE INFO

Article history:
Received 22 August 2019
Received in revised form
13 October 2019
Accepted 25 October 2019
Available online 26 October 2019

ABSTRACT

Three-dimensional interconnected nanoporous graphene (NPG) microfoams and nanofoams are developed via a new approach of solid-state catalytic growth. Both NPG microfoam and nanofoam exhibit similar nanoporous structures that contain close tubular pores and open non-tubular pores but with different particle sizes. As electrochemical reactors for sulfur cathodes, sulfur is encapsulated inside the tubular pores. It is found that NPG nanoreactors can enhance the electrochemical performances in comparison with NPG microreactors, including improved reversible capacities, cyclic performances and rate performances in particular. The electrochemical impedance spectroscopy analysis reveals that NPG nanoreactors facilitate Li^+ transportation and decrease the charge-transfer resistance in comparison with the microreactors, promoting the redox kinetics of multi-step conversions between sulfur and lithium sulfides. This work demonstrates a significant particle size effect of nanoporous graphene on the Li–S electrochemistry and can be useful for designing Li–S batteries as well as other electrochemical energy storage systems.

1. Introduction

Lithium-sulfur (Li–S) batteries possess 3–5 times higher energy density than the conventional Li-ion batteries and can be one of the most promising battery systems. The abundance and low cost of sulfur, being the lightest cathode material [1], endow Li–S batteries with a higher theoretical specific capacity (1167 mA h g^{-1} based on pure Li anode and sulfur cathode) than the state-of-the-art lithium ion batteries (e.g. 117 mA h g^{-1} for $LiC_6|Ni_{1/3}Co_{1/3}Mn_{1/3}O_2$) and possible much lower costs [2–4]. However, there are still a number of challenges for the Li–S batteries including issues from the sulfur cathodes, such as the poor electrical and ionic conductivity of sulfur and lithium sulfides, notorious dissolution and migration of lithium polysulfides species in the conventional liquid ether electrolyte during lithiation and delithiation processes, and volume expansion of sulfur during discharge [5,6]. In combination with issues originated from lithium anode, the as-caused low utilization of sulfur, low energy densities and short service life lead to difficulties in the commercialization of Li–S batteries.

To address the cathodic problems, an effective and common strategy is immobilizing sulfur in porous conductive matrixes [7], which are mostly carbonaceous materials attributed to their low density, high electrical conductivity, high specific surface area (SSA) and good chemical stability [8,9]. For example, the porous carbon materials can not only significantly improve the electrical conductivity of sulfur electrodes, but also can trap the polysulfides species while delaying the migration of polysulfides [10]. Currently, there are various kinds of carbon materials comprising different structures, shapes, sizes, components and forms from macroscopic to nanoscales developed for hosting sulfur [8–14]. The intrinsic features such as microstructure, pore size, pore volume, components, specific surface area and particle sizes of porous carbon could influence the electrochemical performances of sulfur cathodes. Previous works have already proved the influences of pore sizes and pore volume of porous carbon on the energy storage of Li–S batteries [15–21]. Numerous works also reported various carbon hosts including micron-sized to nano-sized particles [8–10,22]. Nevertheless, to the best of our knowledge, it lacks a systematic study of the impact of particle size of the carbon hosts on the electrochemical energy storage of Li–S batteries since the previous studies contained other variables such as large differences in pore sizes or volumes and SSA in addition to the particle size

* Corresponding author.
E-mail address: ewan.lu@rug.nl (L. Lu).

https://doi.org/10.1016/j.carbon.2019.10.072

parameter. Well understanding the particle size effect of the host materials on the electrochemical performances is helpful for designing high-performance sulfur cathodes.

Hypothetically, the particle sizes of these carbon hosts, being as Li–S redox reactors, should have influences on the electrochemical performances. Previous studies showed that, in lithium-ion batteries, reducing the particle size of the active materials can significantly increase the electrochemical reactivity and shorten the diffusion length of Li ions within the particles [23,24]. In a Li–S battery, the dissolution and migration of polysulfides species and poor ionic conductivity of lithium sulfides make the particle size effect more complicated. Recently Zhou et al. pointed out that the particle size of the zeolitic imidazolate framework can balance the internal diffusion and leaching of polysulfides to optimize the reversible capacity and the capacity-decay rate [25]. However, the zeolitic imidazolate framework is not electrically conductive but the most of the porous carbon materials are. This difference hints that the electrons could easily transport to the internal interfaces of sulfur/carbon particle reactors and facilitate the redox reactions. Moreover, zeolitic imidazolate framework mainly contains micropores but many promising porous carbons hosts have a wide pore range from micropores to mesopores and macropores. Considering the differences in the distributions of active materials, transportations of electrons, ions and other polysulfides species, hence the influences of the particle sizes of the electrical-conductive porous carbon hosts on the Li–S reactions are more complicated than in Li-ion batteries and zeolitic imidazolate framework reactors.

For improving the performance of Li–S batteries, nanoporous metal-templated nanoporous graphene (NPG) with 3D interconnected pores have exhibited remarkable potentials ascribed to its intrinsic pores and excellent physical and chemical properties of graphene building blocks [26–28]. Different from the porous graphene made by the self-assembly of reduced graphene oxides [29–31], the 3D interconnected NPG comprises continuously interconnected tubular pores, similar to a winded and jointed carbon nanotube. Its intrinsic porous structure enables encapsulation of sulfur in the tubular pores [17]. Because the particle size of NPG varies the effective length of the interconnected tubular pores, we expect a possible dependence of Li–S reactions on the size of NPG reactors. However, it is a challenge to only change the particle size while keeping other porous characteristics similar in 3D interconnected NPG or other 3D porous carbon materials [32].

In this research, NPG foams are selected as the proof-of-concept prototype to study the particle size effect of reactors on the Li–S electrochemical energy storage. We first develop an approach to synthesize two types of NPG foams, namely NPG microfoams of micron-sized particles and NPG nanofoams of nanometer-sized particles. The synthesis of NPG foams is performed by a catalytic solid-state growth of graphene at low temperature using nanoporous Ni microfoams and nanofoams as templates respectively. Both NPG foams exhibit similar porous characteristics, namely pore size and SSA, but different particle sizes which are on average ~13 μm and 500–1000 nm respectively. The distinct particle sizes selected are aiming to acquire obvious changes of the Li–S reactions and energy storages within the different reactors. The results prove that NPG nanofoams can significantly improve the reversible capacities, cyclic stability and in particular rate performances of the batteries in comparison with the microfoams.

2. Experimental section

2.1. Synthesis of nanoporous Ni microfoams and nanofoams

Nanoporous Ni microfoam templates were prepared by reduction of commercial NiO micron-sized particles at 300 °C for 2 h under H_2/Ar (15% H_2) with a flow rate of 100 sccm [33]. For producing nanoporous Ni nanofoams, NiO nanoparticles were synthesized by thermal decomposition of nickel nitrate hexahydrate at 300 °C for 5 h in the air [34]. After that, the NiO nanoparticles were also reduced under the same condition as for the preparation of the nanoporous Ni microfoams.

2.2. Synthesis of NPG microfoams and nanofoams

The as-obtained nanoporous Ni microfoams and nanofoams were immersed respectively into polyvinylpyrrolidone (PVP, M.W. = 30K) aqueous solution (0.1 g ml^{-1}) for overnight under ultrasonication and stirring. Then the mixtures were kept still for a few hours to let the PVP-coated nanoporous Ni particles deposit on the bottom. After pouring away the top clear solution, the rest mixtures were dried at 60 °C. The dried PVP-coated nanoporous Ni microfoams or nanofoams were heated at 600 °C for 2 h under Ar. After cooling, the graphene-coated nanoporous Ni microfoams or nanofoams were obtained. Then they were put in 1 M $FeCl_3$ solution and kept for 12 h under stirring. Finally, the NPG microfoams or nanofoams were obtained after filtering and washing with DI water repeatedly.

2.3. Synthesis of S-NPG composites

Sulfur (350 mg) was dissolved in carbon disulfide solution, followed by the addition of NPG (150 mg) into the solution and stirring for 2 h. After that, the mixture was dried at 50 °C by evaporating CS_2. The final S-NPG composites were obtained after heating the dried powder at 155 °C for 24 h under Ar protection.

2.4. Materials characterizations

The as-synthesized nanoporous Ni, nanoporous graphene and other products were characterized by scanning electron microscopy (FEI-Philips FEG-XL30s), and high-resolution transmission electron microscopy (JEOL JEM-2010F operated at 200 kV). Raman spectrum analyses were performed using 633 nm laser excitation on a Perkin Elmer Raman station. The electrical conductivity of NPG microfoams and NPG nanofoams was measured by a four-point-probe tester with using Van der Pauw method. Before measurement, the NPG microfoams and NPG nanofoams were carefully compressed into chips at the same pressure.

2.5. Electrochemical measurements

The S-NPG electrode was prepared by making a slurry containing 80 wt% S-NPG composites, 10 wt% carbon black (Fisher Scientific, Super P Conductive, 99+% (metals basis)) and 10 wt% polyvinylidene difluoride (PVDF) binder or PVP binder with NMP (*N*-Methyl-2-Pyrrolidone). The slurry was uniformly spread onto an Al foil and dried. Then the electrode was cut into chips with a diameter of Ø15 mm. The mass loading of active S was ~2.0 mg cm^{-2}. For the assembly of the Li–S batteries, a lithium chip, a Celgard 2500 separator and a working electrode were sealed in a Swagelok-type cell in an argon-filled glovebox (UniLab, Braun, Germany). 1 M lithium bis(tri-fluoromethanesulfonyl) imide (LiTFSI) in 1,3-dioxolane (DOL) and 1,2-dimethoxyethane (DME) (1:1 v/v) with lithium nitrate (3%) was added in each cell and the amount is around 30 μL per milligram of S. The galvanostatic discharge-charge performances were measured under various current densities of 0.1C, 0.2C, 0.5C, 1C, 2C (1C = 1670 mA g^{-1}) within a potential window 1.7–2.8 V. The electrochemical impedance spectroscopy was carried out within the frequency from

100 mHz to 100 kHz with AC amplitude of 5 mV on an electrochemical workstation (CH Instruments Model CHI760e).

3. Results and discussion

Fig. 1 schematically illustrates the catalytic solid-state growth of NPG. The overall synthesis generally comprises three steps: (1) synthesis of nanoporous Ni micron-sized and nano-sized templates by hydrogen reduction of NiO as reported previously [33], (2) solid-state growth of graphene in the assistance of nanoporous Ni catalysts that also serve as templates, (3) etching away the Ni templates. Step 1 and step 2 are the key synthesis procedures. In step 1, the particle sizes and shapes of NiO precursors can remain during reduction so these can determine the particle sizes and shapes of nanoporous Ni templates and further define the NPG foam particles. The pore size and ligament size of nanoporous Ni determine respectively the sizes of the non-tubular pores and tubular pores of NPG foams after etching away the Ni templates. Step 2 mainly involves the growth of graphene on the surface of Ni ligaments. Prior to heating, nanoporous Ni powders are coated with a thin solid organic film such as polyvinylpyrrolidone (PVP) or sugar providing carbon atoms for graphene growth. The heating process enables the thermal decomposition of PVP, followed with catalytic growth of graphene on the Ni ligaments surface [17,35]. As a result, graphene film of controlled thickness is formed on Ni ligaments. The low-temperature range and growth time avoid severe coarsening and guaranty the size retention of Ni ligaments during heating. Adjusting the temperature can also regulate the quality such as crystallinity and defect content of graphene film [17]. Thus, step 2 modifies the microstructures, wall thickness and quality of NPG. The pore volume and specific surface area of NPG were tuned by both step 1 and 2.

Fig. 2 depicts the particle sizes and microstructures of NiO precursors and their corresponding nanoporous Ni particles after reduction. Micron-sized NiO particles mostly are spherical and have a size distribution of 5–20 μm and an average size of 13 μm as shown in Fig. 2a. After reduction, the Ni microparticles remained the shapes and sizes of NiO, but exhibited a porous structure comprising uniform ligaments of ~110 nm thickness and pores (Fig. 2b and c). These pores and ligaments are interconnected and compose three-dimensional micron-sized foams, namely nanoporous Ni microfoams that can be considered as being equivalent to a very long Ni nanowire of 110 nm diameter but knotted, winded and turned into a three-dimensional architecture.

Fig. 2d shows the uniform and ultrafine NiO nanoparticles with octahedral shape. The edge length of Ni octahedral particles is in the range of 500–1000 nm and 700 nm on average. After reduction, nanoporous Ni octahedral nanofoams are obtained as shown in Fig. 2e–f. The average ligament width is similar to that of the microfoams but the length of the ligament is smaller than that of microfoams. In particular, the particle size of Ni nanofoams is about 18 times smaller than that of Ni microfoams. The smaller Ni nanofoams can be considered as a similar-diameter Ni nanowire network but with a shorter length compared to the Ni microfoams. The volume ratio between a spherical particle with a diameter of 13 μm and an octahedral particle with an edge length of 700 nm is above 7000, suggesting a huge length ratio. It should be mentioned that in comparison with dealloying method [36], the hydrogen reduction method seems more facile in procedures because there is no need for complex alloy precursors which usually have complicated textures and the different sizes of grains that lead to hierarchical pores.

Graphene microfoams and nanofoams are obtained via solid-state catalytic growth of graphene on the surface of Ni ligaments and subsequent etching of Ni [17]. Fig. 3 shows the NPG microfoams and nanofoams with sizes and shapes inherited from their corresponding nanoporous Ni templates. Scanning electron microscopy (SEM) micrographs in Fig. 3a and b, Fig. S1 and transmission electron microscopy (TEM) image in Fig. 3c show that NPG microfoams are micron-sized particles and have a porous structure containing two different types of pores. The nontubular open pores inherit from Ni microfoams and the close tubular pores are from the Ni ligaments that are etched off. Both the non-tubular pores and tubular pores construct an interconnected 3D network. The NPG nanofoams also comprise similar tubular pores and nontubular pores that construct a 3D network in nano-sized particles (Fig. 3e–g). High-resolution TEM (HRTEM) observations show that both NPG microfoams and nanofoams have multilayer graphene walls with a thickness of about 7 monolayers (2–3 nm as shown in Fig. 3d and h). Another difference between NPG microfoams and nanofoams is the length of the single tubular pores. The single tubular pores of NPG nanofoams are shorter than those of microfoams due to the smaller sizes and more winded turns. These differences between microfoams and nanofoams should lead to various encapsulations and immobilizations of sulfur in the hosts. With respect to the synthesis approach, the above results fully demonstrate that the low-temperature solid-state catalytic method is well suited for synthesizing NPG microfoams and nanofoams with the same particles sizes and shapes as their porous Ni templates. The good controllability of foam particle sizes and pore sizes

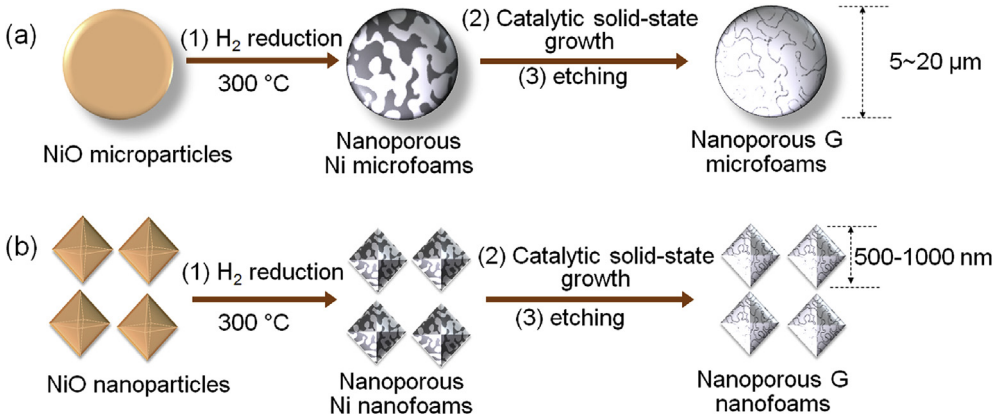

Fig. 1. Schematic illustration of the approach for synthesis of nanoporous graphene (NPG) microfoams and nanofoams. The route includes 3 steps: hydrogen reduction for synthesis of nanoporous Ni, heating nanoporous Ni coated with solid-carbon for solid-state growth of graphene with assistance of nanoporous Ni catalysts, and etching away the Ni templates. Two key synthesis processes are step 1 and 2. (A colour version of this figure can be viewed online.)

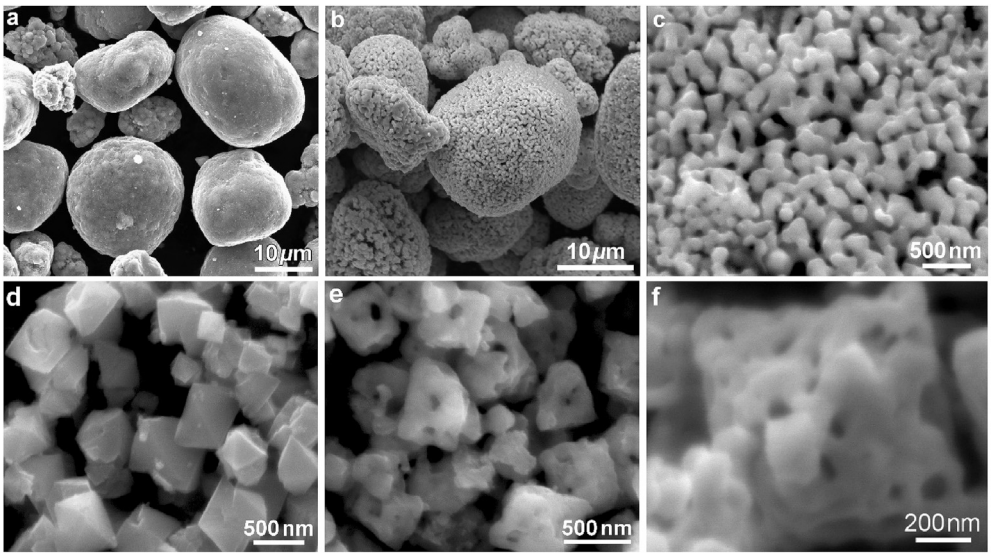

Fig. 2. SEM images of (a) NiO microspheres, (b and c) nanoporous Ni microfoams, (d) NiO octahedral nanoparticles, (e and f) nanoporous Ni nanofoams.

of graphene is mainly attributed to the relatively slow diffusivity of metal atoms and suitable catalytic growth of graphene on Ni at low temperatures (i.e. 600 °C) in comparison with high-temperature chemical vapor deposition approaches (i.e. >900 °C) [37]].

The quality of the NPG microfoams and nanofoams is examined by Raman spectroscopy, as shown in Fig. 4a. The Raman spectra of both NPG microfoams and nanofoams exhibit the G band at ~1585 cm^{-1} and D band at ~1325 cm^{-1}. The ratio between the D and G peak intensities (I_D/I_G) reveals the defects content. The I_D/I_G of microfoams and nanofoams is 1.33 and 1.36 respectively, which is higher than that of reported NPG synthesized at 700 °C and 800 °C also by the solid-sate catalytic growth [17]. It indicates that microfoams and nanofoams contain many defects, reflecting that the growth temperature is very crucial for graphene crystallinity. The spacing between point defects of graphene, L_D, can be estimated based on the following equation [38]:

$$L_D^2\left(nm^2\right) = (1.8\pm0.5)\times 10^{-9}\lambda^4\left(\frac{I_D}{I_G}\right)^{-1} \quad (1)$$

where λ is the wavelength of the laser beam (in nanometer). By substituting the I_D/I_G ratios of microfoams and nanofoams, L_D is calculated in the range of 12.5–16.7 nm for microfoams and 12.3–16.5 nm for nanofoams, respectively. Further, the defect density $n_D(cm^{-2})$ can be calculated in the range of (1.1–1.9)*10^{11}/cm^2 (1100–1900/μm^2) for both microfoams and nanofoams according to the following equation [38]:

$$n_D\left(cm^{-2}\right) = \frac{(1.8\pm0.5)\times 10^{22}}{\lambda^4}\left(\frac{I_D}{I_G}\right) \quad (2)$$

Fig. 4b displays the nitrogen adsorption-desorption isotherm of NPG microfoams and nanofoams. The Brunauer-Emmett-Teller (BET) SSA of NPG microfoams and nanofoams are 310 and 331 $m^2\,g^{-1}$, respectively. According to the Barrett–Joyner–Halenda (BJH) adsorption, the average pore size for NPG microfoams and nanofoams are both ~17 nm. The total pore volumes are 1.1 and 1.3 $cm^3\,g^{-1}$, respectively, for NPG microfoams and nanofoams. The steep uptake in the range $p/p_0 < 0.01$ in the N_2 sorption isotherm indicates the existence of abundant micropores that comprise the defects. The hysteresis loop at $0.43 < p/p_0 < 1$ exhibits no limiting adsorption at high p/p_0 and no clear boundary between the sorption regions corresponding to the meso- and macro-pores (2–110 nm). The above results demonstrate that the NPG microfoams and nanofoams have similar porous characteristics.

The electrical conductivity of NPG microfoams and nanofoams is also analyzed. Both NPG microfoams and NPG nanofoams have good electrical conductivities (see Fig. S2). As the NPG microfoam and nanofoam have similar defects content, crystallinity and porous structure, theoretically the electrical conductivity of NPG microfoam and nanofoam should be the same. However, a compressed chip of NPG microfoams has higher bulk electrical conductivity ($24\pm3\ S\,cm^{-1}$) than that of a chip of NPG nanofoams ($4\pm1\ S\,cm^{-1}$). This can be ascribed to the higher content of particle boundaries in the NPG nanofoams chip than that in the NPG microfoams chip.

Cathodic materials of sulfur and lithium sulfides have poor electronic and ionic conductivity, severe dissolution and migration of lithium polysulfides species in the conventional liquid electrolyte and volume expansion of sulfur after discharge [1,2,5–7]. Nanoporous graphene microfoams and nanofoams can be promising reactors for lithium-sulfur electrochemical reactions. The encapsulation of sulfur in NPG is performed by the infiltration of molten sulfur method. Driven by capillary forces, liquid sulfur infiltrates through the tubular pores of NPG. After solidification, liquid sulfur shrinks to form uniform sulfur nanoparticles within the tubular pores. All the S-NPG composites have a similar sulfur content of around 69 wt% as confirmed by thermodynamic analysis (TGA) shown in Fig. S3 of Supporting information. Further investigations on the microstructure of S-NPG composites are carried out by electron microscopy. Fig. 5a and b show the microstructure of S-NPG microfoam composite. Sulfur particles are completely encapsulated in the tubular pores of NPG instead of deposition in non-tubular open pores. The uniformity of sulfur distribution is shown in Fig. 5b with energy-dispersive X-ray spectroscopy (EDS) mapping of C and S. TEM observations in Fig. 5c and d reveal sulfur nanoparticles encapsulated in the tubular pores. From Fig. 5d, the sulfur particles wrapped by graphene layers can be clearly seen, indicating the intimate contact between sulfur and graphene wall. Similarly, there is no sulfur deposit on the outer surface of tubular pores for S-NPG nanofoams (Fig. 5e). The TEM micrographs in Fig. 5f and g depict the distribution of sulfur nanoparticles in the tubular pores of NPG nanofoams. HR-TEM image in Fig. 5h also

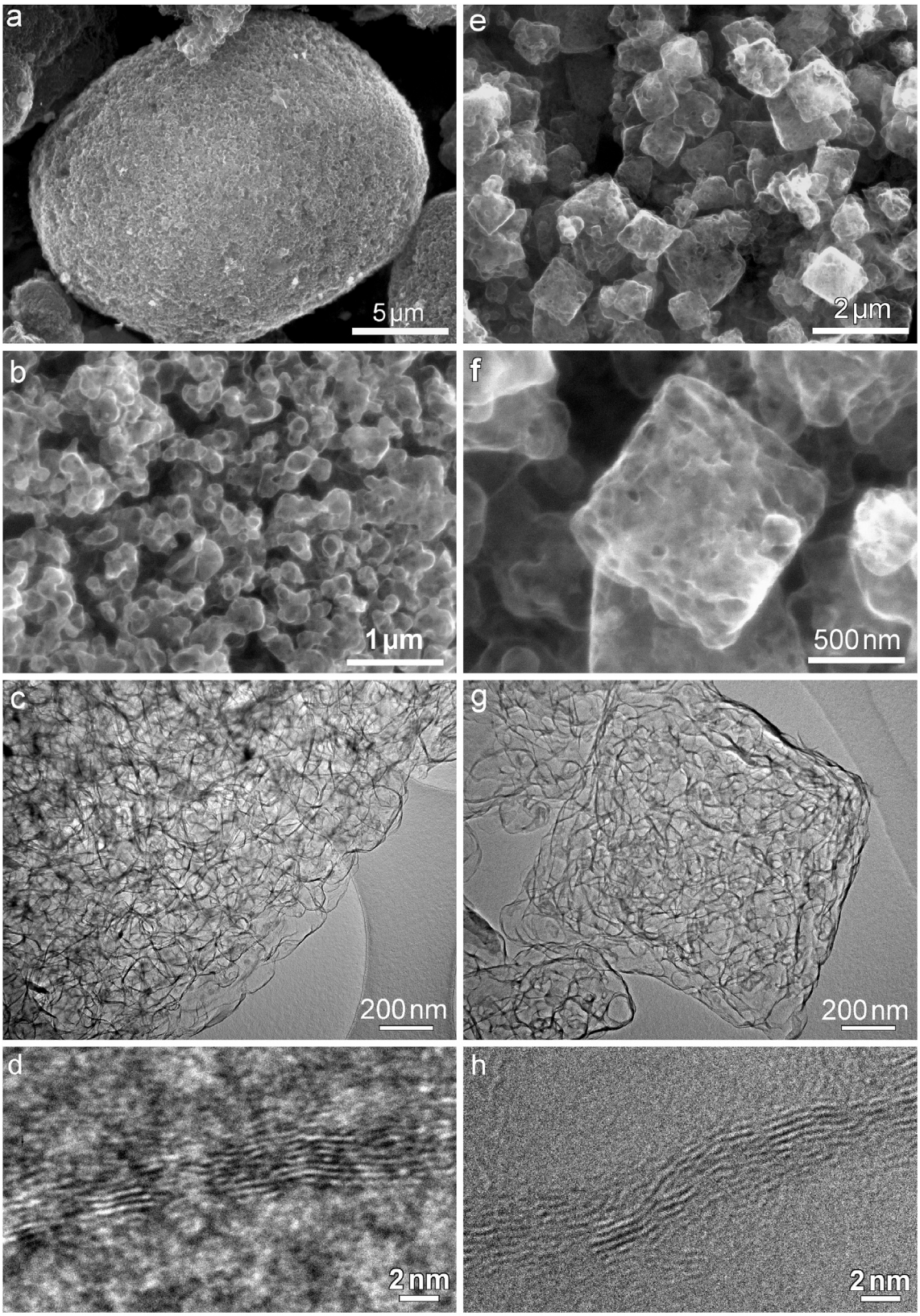

Fig. 3. (a, e) SEM micrographs showing NPG microfoam particles (left column) and NPG nanoform particles (right column); (b, f) SEM micrographs and (c, g) TEM images showing the porous structure of NPG microfoam and nanofoam; (d, h) HRTEM images showing graphene layers and wall thickness of NPG microfoam and nanofoam.

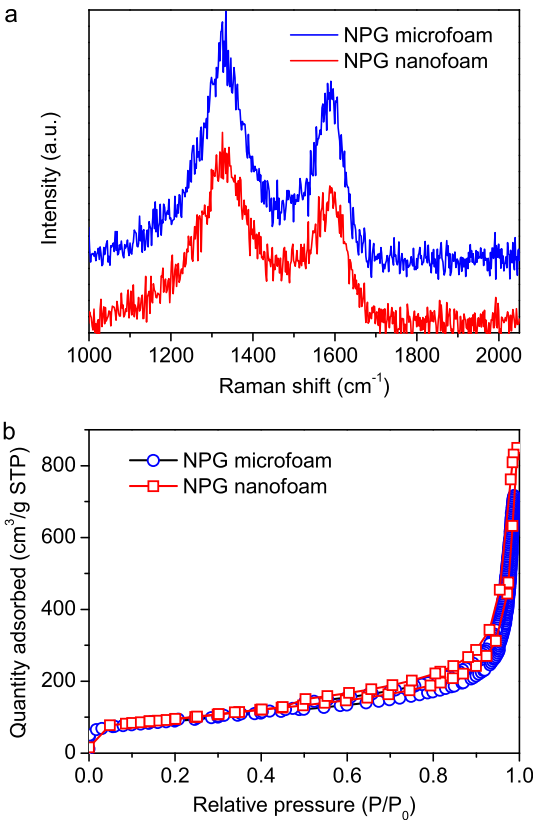

Fig. 4. (a) Raman spectrum and (b) N_2 adsorption–desorption isotherms of microfoam and nanofoam. (A colour version of this figure can be viewed online.)

demonstrates the close contact between sulfur and graphene. The nitrogen adsorption-desorption isotherm of S-NPG microfoam and nanofoam composites confirm their similar porous features (see Fig. S4 in the Supplementary information) and SSA of around 44 $m^2 g^{-1}$.

To evaluate the lithiation and delithiation processes of the S-NPG microfoam and nanofoam composites, the S-NPG composites are prepared as a cathode which is then paired with a lithium electrode in the cell for electrochemical investigations. The galvanostatic discharge and charge under different current densities from 0.05 to 2C (1C = 1670 mA/g) are carried out within the voltage window of 1.7–2.8 V for measuring the specific capacities (based on sulfur) and cyclic stabilities. Fig. 6a shows the initial galvanostatic discharge/charge profiles of the S-NPG microfoam and nanofoam composites at various current densities. Generally, during lithiation the reductions occur at two plateaus that are at 2.4–2.1 V and 2.1–1.7 V, corresponding to the conversion from cyclic octa-atomic sulfur (S_8) to long-chain polysulfide anions ($S_8 \rightarrow Li_2S_x$, x = 4–8) and from long-chain polysulfides to lithium sulfide ($Li_2S_4 \rightarrow Li_2S_2 \rightarrow Li_2S$), respectively [1,2,5]. The upper-plateau reaction contributes ~25% of the overall capacity (Q_H: theoretical value = 419 mA h g^{-1} based on sulfur) while the lower-plateau reaction providing ~75% (Q_L: theoretical value = 1256 mA h g^{-1}). At 0.05C, both S-NPG microfoam and nanofoam composite electrodes exhibit high initial capacities of discharge and charge (1246 and 1091 mA h g^{-1} for S-NPG microfoam, 1285 and 1172 mA h g^{-1} for S-NPG nanofoam). The high utilization of sulfur of the composite cathodes is ascribed to the high SSA, electrical conductivity and unique interconnected porous structure of NPG nanofoams and microfoams. At 0.1C, the capacity decreases slightly for S-NPG nanofoam but drops rapidly for the S-NPG microfoam. With increasing the current density further, the capacity continues to decline. Meanwhile, the polarizations behave seriously. The polarizations are affected more slightly for S-NPG nanofoam than those of S-NPG microfoam, especially when increasing the current density from 0.2C to 2C. In particular, although there are severe polarizations at 1C and 2C, the discharge reaction between Li and S-NPG nanofoam still contains multi-step reduction of sulfur, i.e. upper-plateau and lower-plateau reaction. In contrast, S-NPG microfoam only displays the upper-plateau reduction, indicating more severe polarizations. Thus, the particle sizes of the hosting materials can affect the polarization at high rates (e.g. 0.5–2C).

We further evaluate the two-plateau electrochemical reactions in both S-NPG microfoam and nanofoam composite electrodes, and the discharge capacities Q_H and Q_L of the electrodes at various current densities are calculated and shown in Fig. 6b. With increasing the current density, all Q_H and Q_L decrease. For both S-NPG microfoam and nanofoam composite electrodes their Q_L decrease faster than their Q_H respectively, indicating that the low–plateau reaction mainly caused the capacity drop at high rates. Comparing to the S-NPG microfoams, the S-NPG nanofoams remain higher in capacities that decrease significantly less. The Q_H and Q_L of S-NPG nanofoams decrease more slowly than those of the S-NPG microfoams, particularly at high current densities from 0.5C to 2C. This observation is clearer when looking through the Q_L at high rates. At high rates from 0.5C to 2C $Q_{L:nanofoams}$ gradually decreases. In contrast, at 0.5C $Q_{L:microfoams}$ dramatically drops and becomes 0 at 1C and 2C. Individually, for S-NPG nanofoams mainly Q_L affects the overall capacity as Q_H only decreases slightly. While for composite microfoams, both dramatic decreases of Q_H and Q_L in particularly at high current densities cause the rapid decline of overall capacity.

These results reflect that the nano- and micro-foams differ in the two-plateau electrochemical reactions. It is known that the upper-plateau electrochemical reaction is a kinetically fast solid-to-liquid reaction, while the lower-plateau is a slow liquid-to-solid reaction kinetically [39]. For both of the composite cathodes, the slower decreases of Q_H than Q_L are in good agreement with the faster solid-to-liquid reaction than liquid-to-solid reaction. But both Q_H and Q_L for nanofoam cathodes decrease slower than those of microfoam cathodes, suggesting that the nanofoam cathodes hold both faster solid-to-liquid and liquid-to-solid reactions than microfoam electrodes. It also reflects that for S-NPG nanofoams mainly the slow liquid-to-solid reaction limits the rate performances but both the solid-to-liquid and liquid-to-solid reactions do so for S-NPG microfoams.

Fig. 6c illustrates the rate performances of the S-NPG composites. At 0.1C, the capacities for S-NPG nanofoams and microfoams electrodes are 1143 and 1050 mA h g^{-1} for discharging and 1077 and 996 mA h g^{-1} for charging, respectively. With increasing the current density, the discharge capacities of S-NPG nanofoams gradually decrease and stabilize at around 822, 719, 560, 382 mA h g^{-1} for rates at 0.2, 0.5, 1 and 2C, respectively. When the rate returns to 0.5C, the capacity returns to 720 mA h g^{-1}. In contrast, the discharge capacity of S-NPG microfoams decreases faster and stabilizes at much lower values of 704, 305, 134, 54 mA h g^{-1} for rates at 0.2, 0.5, 1 and 2C, respectively. Consistent with the above results, the S-NPG microfoams exhibit poorer performances at high rates. When the current density returns to 0.5C, the capacity only returns to around 300 mA h g^{-1}.

Long-term cyclic performances at high rates are studied in order to assess the capacity stability of S-NPG microfoams and nanofoams. Fig. 6d demonstrates the cyclic performances of S-NPG composites at 0.2C. To achieve full activation of sulfur, all cells are initially discharged and charged at 0.05C. The first discharge and charge capacities of the S-NPG nanofoams electrode are 929 and

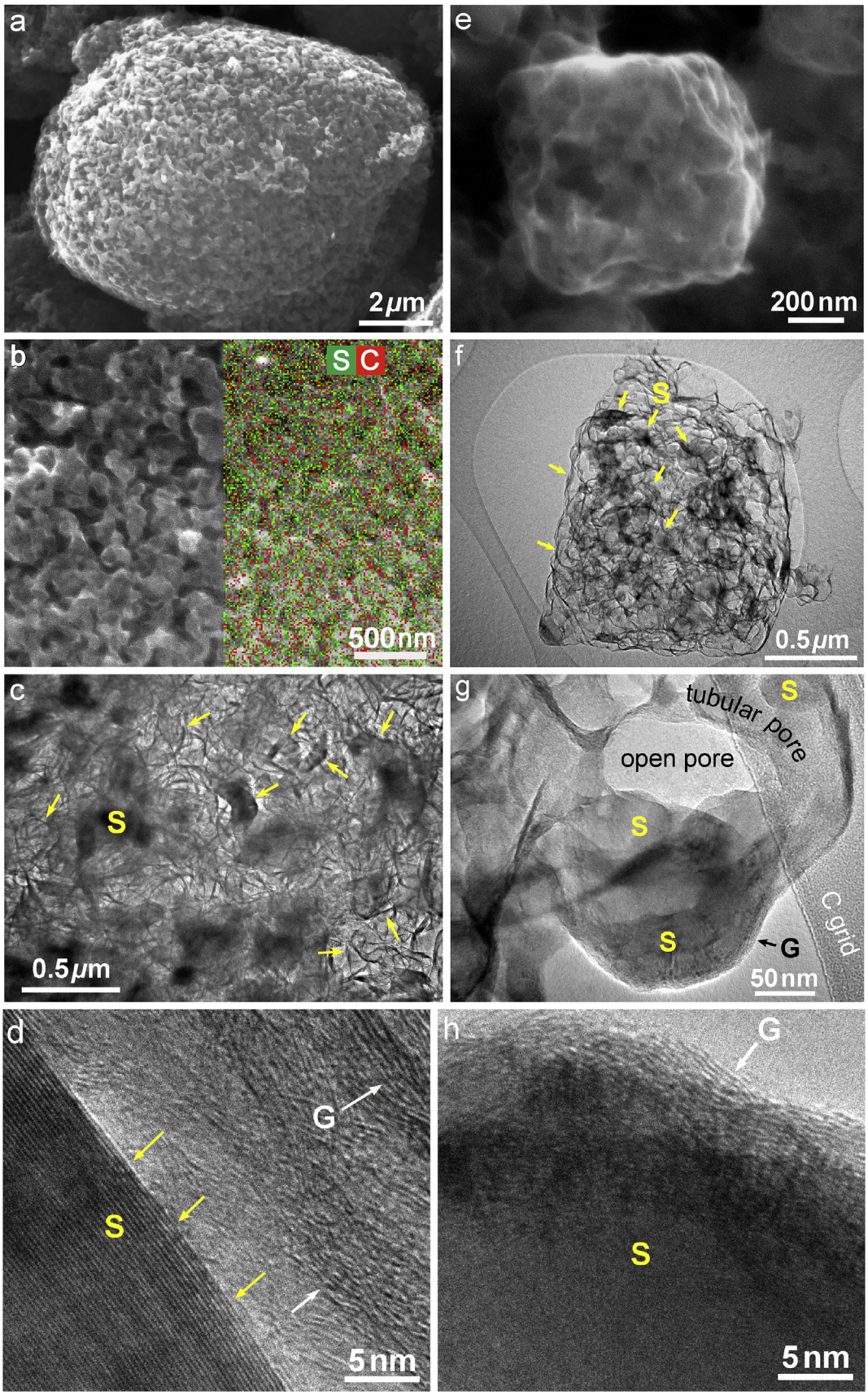

Fig. 5. (a) SEM image of S-loaded NPG microfoam particle, (b) SEM micrograph of high magnification showing uniformly encapsulated S in the tubular pores of NPG microfoam confirmed with element mapping of C and S, (c, d) TEM and HRTEM images revealing encapsulation of S particles in NPG microfoam; (e) SEM image of S-NPG nanofoam particle, (f, g) TEM and (h) HRTEM images showing homogeneously encapsulated S particles in NPG nanofoam. (A colour version of this figure can be viewed online.)

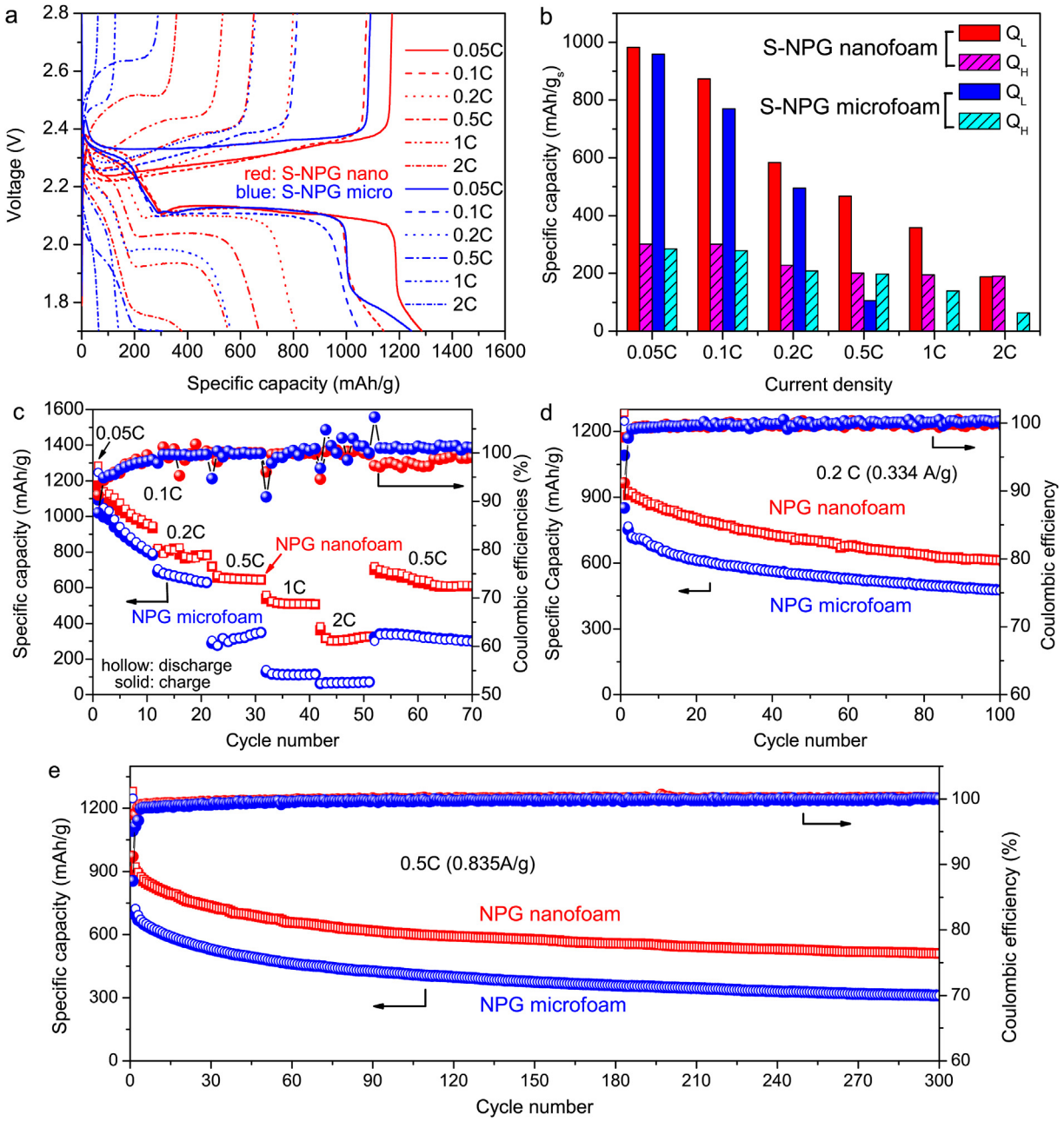

Fig. 6. (a–c) Voltage profiles, the capacities contributed from upper-plateau and lower-plateau reactions, discharge/charge capacities and Coulombic efficiency of the S-NPG composite cathodes cycled between 1.7 and 2.8 V under different current densities from 0.05C to 2C; (d and e) discharge/charge capacities and of Coulombic efficiency of the S-NPG composite cathodes at 0.2C and 0.5C rate. (A colour version of this figure can be viewed online.)

910 mA h g^{-1}. After 100 cycles, the reversible capacities decrease to 613 mA h g^{-1}. The capacity retention is 66% and the average decay rate is 0.34%/cycle. In contrast, the S-NPG microfoams electrode has a lower initial reversible capacity of 768 mA h g^{-1}, and decrease to 476 mA h g^{-1} after 100 cycles. The average decay rate is 0.38%/cycle, which is higher than that of S-NPG nanofoams. Furthermore, Fig. 6e shows the cyclic stability at 0.5C. The initial discharge capacity of the S-NPG nanofoams electrode is 923 mA h g^{-1}, remained at 510 mA h g^{-1} after 300 cycles. The capacity decay is only 0.15% per cycle. Comparing with the S-NPG nanofoams electrode, the S-NPG microfoams electrode shows a lower capacity of 724 mA h g^{-1} at the initial cycle and 310 mA h g^{-1} at the 300th cycle, leading to an average decay rate of 0.19%/cycle. These results show improved cyclic stability and higher reversible capacity over long-term cycling of the S-NPG nanofoams in comparison with S-NPG microfoams. With respect to the relatively large initial capacity decay (particularly in the first 50 cycles) at 0.2 C and 0.5C, it is assumed that many defects as revealed with Raman analysis could induce holes on NPG walls that allow partial dissolution of polysulfides. Compared to other 3D interconnected porous graphene/S cathodes, the NPG nanofoams can be regarded as a promising material for encapsulation of sulfur for lithium–sulfur batteries with high utilization and cyclic stability of active materials (Table S1 of Supporting Information).

In order to understand more deeply the causes for the different performances between the S-NPG nanofoam and microfoam

cathodes, electrochemical impedance spectroscopy (EIS) is performed to detect the reaction kinetics of conversions between sulfur and lithium sulfide within the NPG nanofoams and the microfoams. Different electrochemical reactions kinetics can be reflected from the observations that Q_H and Q_L behave differently with varying rates at the discharge potentials 2.4–2.1 V and 2.1–1.7 V. EIS spectra of discharged batteries at 2.25 V and 1.7 V are detected to affirm the charge transfer resistance (R_{ct}) and diffusivity of Li^+ through the phases of lithium-sulfur compounds. The impedance plots of batteries at 2.25 V as shown in Fig. 7a are composed of one semicircle in the high-frequency region and one semicircle in the medium-frequency region that are corresponding to the charge transfer resistance at the interfaces of soluble polysulfides (R_{ct1}) and of solid lithium polysulfides (R_{ct2}), respectively [40]. The slope line in the low-frequency region is assigned to the diffusion of Li^+ within lithium polysulfides. The S-NPG nanofoams electrode delivers smaller R_{ct1} (61 Ω) and R_{ct2} (34 Ω) than the S-NPG microfoams (121 Ω for R_{ct1} and 68 Ω for R_{ct2} respectively), indicating smaller charge-transfer resistances of smaller particle sizes. Fig. 7b shows the impedance spectra of the cells at 1.7 V. The plots only contain one semicircle in the high-frequency region corresponding to charge transfer resistance at the interfaces of Li_2S (R_{ct3}) and one slope line in the low-frequency region assigned to the diffusion of Li^+ within lithium sulfides. The calculated R_{ct3} for the S-NPG nanofoams and microfoams electrodes is 26 Ω and 77 Ω, respectively, which demonstrates the discharge product of the S-NPG nanofoams electrode having less charge transfer resistances than the discharge product of the S-NPG microfoams electrode.

In addition, the diffusivity of Li^+ (D) can be obtained as below [41]:

$$D = 0.5\left(\frac{RT}{An^2F^2\sigma C}\right)^2 \tag{3}$$

where R is the gas constant, T is the temperature (298.5 K), A is the area of the electrode surface, n is the number of electrons involved (as illustrated in Supplementary Information), F is Faraday's constant, σ is the Warburg coefficient and C is the molar concentration of Li^+ in the electrolyte. In Warburg region, Z_{re} has a linear relationship with the reciprocal root square of the lower angular frequencies ($\omega^{-0.5}$) as shown in Eq. (4), and σ can thus be obtained by the slope of the linear plot [42]:

$$Z_{re} = R_e + R_{ct} + \sigma\omega^{-0.5} \tag{4}$$

where R_e is the resistance of the electrolyte, R_{ct} is the charge transfer resistance, ω is the angular frequency. A larger slope σ reflects a higher diffusion resistance. The linear relationships between Z_{re} and $\omega^{-0.5}$ for the samples of S-NPG nanofoams and microfoams at 2.25 V and 1.7 V are shown in Fig. 7c and d. The Warburg coefficients of the S-NPG nanofoams electrode are smaller than those of the S-NPG microfoams electrode. Through Eq. (3) and Eq. (4), the ratio of diffusivities of Li^+ at 2.25 V and 1.7 V between the S-NPG nanofoams electrode and S-NPG microfoams electrode can be obtained as shown in Eq. (5) and Eq. (6).

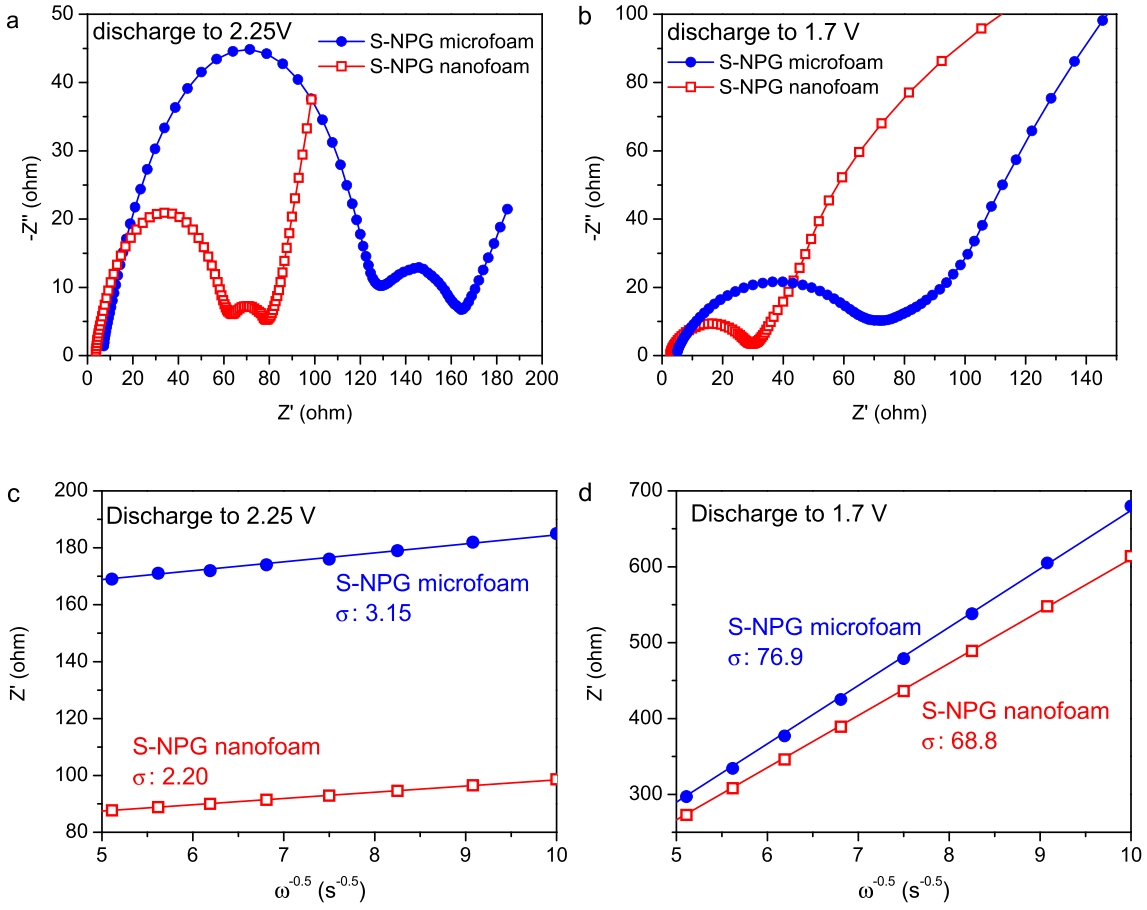

Fig. 7. EIS spectra of cells with S-NPG microfoams and nanofoams cathodes at different stages: (a) discharge to 2.3 V, (b) discharge to 1.7 V, (c and d) the relationship between Z′ and $\omega^{-1/2}$ at low frequencies for S-NPG composite electrodes discharged at 2.25 V and 1.7 V, respectively. (A colour version of this figure can be viewed online.)

$$\text{At } 2.25 \text{ V}, \frac{D(Li^+)_{nano}}{D(Li^+)_{micro}} = \left(\frac{\sigma_{micro}}{\sigma_{nano}}\right)^2 = \left(\frac{3.15}{2.2}\right)^2 = 2.05 \quad (5)$$

$$\text{At } 1.7 \text{ V}, \frac{D(Li^+)_{nano}}{D(Li^+)_{micro}} = \left(\frac{\sigma_{micro}}{\sigma_{nano}}\right)^2 = \left(\frac{76.9}{68.8}\right)^2 = 1.25 \quad (6)$$

It reveals that the S-NPG nanofoams electrode has higher diffusivities of Li^+ within both long-chain lithium polysulfides when discharging at 2.25 V and lithium sulfides when discharging at 1.7 V than the S-NPG microfoams electrode. The decreased interfacial charge transfer resistances and improved diffusivities of Li^+ fully explain the enhanced electrochemical performances such as the utilization of sulfur (reversible capacity), rate performances, and polarizations of S-NPG nanofoams cathode in comparison with the S-NPG microfoams cathode. It also proves that the diffusion coefficient of Li^+ ions within lithium sulfides is much smaller than that in lithium long-chain polysulfides. This causes a rapid decline of Q_L than Q_H at the high rates and is in agreement with the observations from Fig. 6b.

From a comprehensive view, both the NPG nanofoams and microfoams have similar microstructures, quality, porosities but different particles sizes. According to the EIS analysis, similar internal resistances of the cells are also observed for two composites. In combination with the electrical conductivity analyses (Fig. S2), it implies that the main cause of the different electrochemical performances between the microfoams and nanofoams is not the electron transportation but the effect of NPG foam particle size. Fig. 8 shows a schematic model depicting how the particle size of 3D NPG micro- and nano-reactors affects the electrochemical performances. The interconnected NPG micro-/nano-foams can be considered as networks constituted by knotted, winded and turned tubular graphene with a diameter of 110 nm as revealed in Fig. 3. In this way an NPG microfoam can be equivalent to a long tubular graphene while a smaller nanofoam is equivalent to a shorter tubular graphene. Thus the length and volume ratios between a microfoam and a nanofoam are of huge difference. Due to the considerable large pore length of the microfoam reactors, Li^+ ions suffer from a relatively high diffusion resistance within the rather long tubular pores. In contrast, the nanofoam reactors have a much smaller length of tubular pores, shorten the pathways of ions transport and particularly facilitate the rate performances. The small particle sizes and short tubular pores also facilitate a more homogeneous distribution of sulfur which can be seen from Fig. 5, leading to smaller charge-transfer resistances in the S-NPG nanofoams than those in the S-NPG microfoams. The overall particle size effects cause higher reversible capacities, better rate performances and cyclic stabilities of S-NPG nanofoams than those of S-NPG microfoams.

4. Conclusion

3D bicontinuously NPG microfoams and nanofoams are synthesized via a new solid-state catalytic growth method using nanoporous Ni templates. Both NPG microfoams and nanofoams comprise a similar porous structure (e.g. non-tubular pores and tubular pores with comparable diameters), wall thicknesses and defect contents, but with different particle sizes and shapes. By encapsulation of sulfur in the tubular pores of NPG microfoams and nanofoams, the S-NPG composites exhibit different reversible capacities and cycling performances. The S-NPG nanofoam composite cathode outperforms in particular under high rates. Based on the EIS analyses, the smaller particle sizes of NPG nanofoams can shorten the diffusion length of ions, increase the diffusion coefficient of Li^+ and decrease the transfer resistances, resulting in faster redox kinetics. It is concluded that the particle size of the sulfur host is an important parameter for designing sulfur cahodes, which can lead to large differences in energy density, power density and lifespan of batteries.

In addition, this work provides a method for synthesizing NPG micro- or nano-foams with controllable particle sizes and pore sizes, as one of the current challenges is the synthesis of well-defined metallic templates. This work also provides guidelines for designing high-performance sulfur cathodes using graphene and other conductive micro/nano-porous materials. The as-developed nanoporous graphene nanofoams and microfoams could be also used for other electrodes such as lithium anodes and other devices such as supercapacitors.

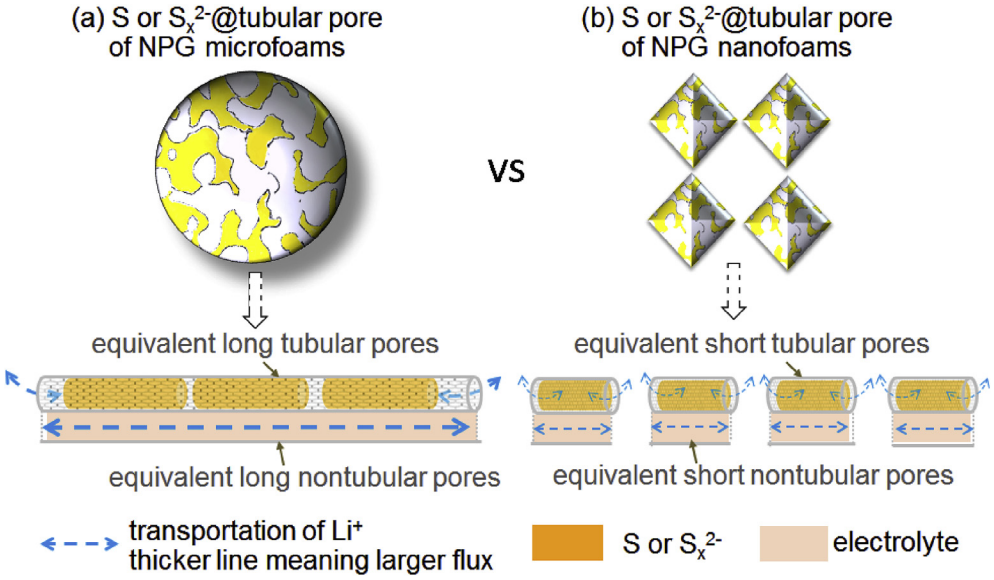

Fig. 8. Simplified schematic model of S or S_x^{2-} (intermediate or final discharge products)@tubular pores of NPG microfoams and @tubular pores of nanofoams. The utilization of sulfur and rate performances are determined by the length of equivalent tubular pores and diffusion resistance of Li^+ within the tubular pores.

Declaration of competing interest

The authors declare no conflict of interest.

Acknowledgement

The authors gratefully acknowledge the financial support from the Faculty of Science and Engineering, University of Groningen, The Netherlands. We also sincerely thank Professor Wesley R. Browne for valuable discussion and support to the Raman analysis of nanoporous graphene samples.

Appendix A. Supplementary data

Supplementary data to this article can be found online at https://doi.org/10.1016/j.carbon.2019.10.072.

References

[1] Z.W. Seh, Y.M. Sun, Q.F. Zhang, Y. Cui, Designing high-energy lithium–sulfur batteries, Chem. Soc. Rev. 45 (2016) 5605–5634.
[2] A. Manthiram, S.H. Chung, C.X. Zu, Lithium–sulfur batteries: progress and prospects, Adv. Mater. 27 (2015) 1980–2006.
[3] A. Eftekhari, On the theoretical capacity/energy of lithium batteries and their counterparts, ACS Sustain. Chem. Eng. 7 (2019) 3684–3687.
[4] A. Eftekhari, Lithium batteries for electric vehicles: from economy to research strategy, ACS Sustain. Chem. Eng. 7 (2019) 5602–5613.
[5] Q. Pang, X. Liang, C.Y. Kwok, L.F. Nazar, Advances in lithium–sulfur batteries based on multifunctional cathodes and electrolytes, Nat. Energy 1 (2016), 16132.
[6] M. Wild, L. O'Neill, T. Zhang, R. Purkayastha, G. Minton, M. Marinescub, G.J. Offer, Lithium sulfur batteries, a mechanistic review, Energy Environ. Sci. 8 (2015) 3477–3494.
[7] H.J. Peng, J.Q. Huang, X.B. Cheng, Q. Zhang, Review on high-loading and high-energy lithium-sulfur batteries, Adv. Energy Mater. 7 (2017), 1700260.
[8] A. Eftekhari, D.W. Kim, Cathode materials for lithium–sulfur batteries: a practical perspective, J. Mater. Chem. A 5 (2017) 17734–17776.
[9] L.L. Zhang, Y.J. Wang, Z.Q. Niu, J. Chen, Advanced nanostructured carbon-based materials for rechargeable lithium-sulfur batteries, Carbon 141 (2019) 400–416.
[10] O. Ogoke, G. Wu, X.L. Wang, A. Casimir, L. Ma, T.P. Wu, J. Lu, Effective strategies for stabilizing sulfur for advanced lithium–sulfur batteries, J. Mater. Chem. A 5 (2017) 448–469.
[11] X.L. Ji, K.T. Lee, L.F. Nazar, A highly ordered nanostructured carbon–Sulphur cathode for lithium–sulphur batteries, Nat. Mater. 8 (2009) 500–506.
[12] S. Choudhury, M. Zeiger, P. Massuti-Ballester, S. Fleischmann, P. Formanek, Lars Borchardt, V. Presser, Carbon onion–sulfur hybrid cathodes for lithium–sulfur batteries, Sustain. Energy Fuels 1 (2017) 84–94.
[13] B. Kruner, T.S. Dorr, H. Shim, J. Sann, J. Janek, V. Presser, Gyroidal porous carbon activated with NH_3 or CO_2 as lithium-sulfur battery cathodes, Batter. Supercaps 1 (2018) 1–13.
[14] S.-Z. Zeng, X. Zeng, W. Tu, Y. Yao, L. Yu, H. Wu, W. Jin, H. Huang, J. Zou, Facile and tailored synthesis of ultrahigh-surface area clews of carbon nanobelts for high-rate lithium–sulfur batteries, J. Mater. Chem. A 5 (2017) 23209–23220.
[15] W.D. Zhou, C.M. Wang, Q.L. Zhang, H.D. Abruña, Y. He, J.W. Wang, S.X. Mao, X.C. Xiao, Tailoring pore size of nitrogen-doped hollow carbon nanospheres for confining sulfur in lithium-sulfur batteries, Adv. Energy Mater. 5 (2015), 1401752.
[16] C.Y. Zhao, L.J. Liu, H.L. Zhao, A. Krall, Z.H. Wen, J.H. Chen, P. Hurley, J.W. Jiang, Y. Li, Sulfur-infiltrated porous carbon microspheres with controllable multimodal pore size distribution for high energy lithium–sulfur batteries, Nanoscale 6 (2014) 882–888.
[17] L.Q. Lu, N. Schriever, J.ThM. De Hosson, Y.T. Pei, Low-temperature solid-state growth of three-dimensional bicontinuous nanoporous graphene with tunable porosity for lithium–sulfur batteries, J. Mater. Chem. A 6 (2018) 11405–11415.
[18] F. Hippauf, W. Nickel, G.-P. Hao, K. Schwedtmann, L. Giebeler, S. Oswald, L. Borchardt, S. Doerfler, J.J. Weigand, S. Kaskel, The importance of pore size and surface polarity for polysulfide adsorption in lithium sulfur batteries, Adv. Mater. Interfaces 3 (2016), 1600508.
[19] W. Deng, X.F. Zhou, Q.L. Fang, Z.P. Liu, Graphene/sulfur composites with a foam-like porous architecture and controllable pore size for high performance lithium-sulfur batteries, ChemNanoMat 2 (2016) 952–958.
[20] C. Wang, L.S. Sun, X.X. Wang, L.M. Wang, Spherical hybrid hierarchical porous structure: a plastic model with tunable inner pores for lithium-sulfur batteries, Carbon 153 (2019) 691–698.
[21] S. Wang, Z.X. Zhao, H. Xu, Y.F. Deng, Z. Li, G.H. Chen, Sulfur impregnated in tunable porous N-doped carbon as sulfur cathode: effect of pore size distribution, Electrochim. Acta 173 (2015) 282–289.
[22] X.Y. Long, Z.F. Zhang, Y. Huang, Y.S. Chen, Sulfur-infiltrated graphene-based layered porous carbon cathodes for high-performance lithium–sulfur batteries, ACS Nano 8 (2014) 5208–5215.
[23] P. Poizot, S. Laruelle, S. Grugeon, L. Dupont, J.-M. Tarascon, Nano-sized transition-metal oxides as negative-electrode materials for lithium-ion batteries, Nature 407 (2000) 496–499.
[24] P.G. Bruce, B. Scrosati, J.M. Tarascon, Nanomaterials for rechargeable lithium batteries, Angew. Chem. Int. Ed. 47 (2008) 2930–2946.
[25] J.W. Zhou, X.S. Yu, X.X. Fan, X.J. Wang, H.W. Li, Y.Y. Zhang, W. Li, J. Zheng, B. Wang, X.G. Li, The impact of the particle size of a metal–organic framework for sulfur storage in Li–S batteries, J. Mater. Chem. A 3 (2015) 8272–8275.
[26] Y. Ito, Y. Tanabe, H.J. Qiu, K. Sugawara, S. Heguri, N.H. Tu, K.K. Huynh, T. Fujita, T. Takahashi, K. Tanigaki, M.W. Chen, High-quality three-dimensional nanoporous graphene, Angew. Chem. 126 (2014) 4922–4926.
[27] G.M. Zhou, L. Lia, C.Q. Ma, S.G. Wang, Y. Shi, N. Koratkar, W.C. Ren, F. Li, H.M. Cheng, A graphene foam electrode with high sulfur loading for flexible and high energy Li-S batteries, Nano Energy 11 (2015) 356–365.
[28] Y. Wu, J. Zhu, L. Huang, A review of three-dimensional graphene-based materials: synthesis and applications to energy conversion/storage and environment, Carbon 143 (2019) 610–640.
[29] Y. Zhao, J. Liu, Y. Hu, H.H. Cheng, C.G. Hu, C.C. Jiang, L. Jiang, A.Y. Cao, L.T. Qu, Highly compression-tolerant supercapacitor based on polypyrrole-mediated graphene foam electrodes, Adv. Mater. 25 (2013) 591–595.
[30] R.J. Zhang, Y.C. Cao, P.X. Li, X.B. Zang, P.Z. Sun, K.L. Wang, M.L. Zhong, J.Q. Wei, D.H. Wu, F.Y. Kang, H.W. Zhu, Three-dimensional porous graphene sponges assembled with the combination of surfactant and freeze-drying, Nano Res. 7 (2014) 1477–1487.
[31] Z.Q. Niu, J. Chen, H.H. Hng, J. Ma, X.D. Chen, A leavening strategy to prepare reduced graphene oxide foams, Adv. Mater. 24 (2012) 4144–4150.
[32] K. Chen, L.R. Shi, Y.F. Zhang, Z.F. Liu, Scalable chemical-vapour-deposition growth of three-dimensional graphene materials towards energy-related applications, Chem. Soc. Rev. 47 (2018) 3018–3036.
[33] L.Q. Lu, P. Andela, J.T.M. De Hosson, Y.T. Pei, Template-free synthesis of nanoporous nickel and alloys as binder-free current collectors of Li-ion batteries, ACS Appl. Nano Mater. 1 (2018) 2206–2218.
[34] G.X. Tong, Q. Hu, W.H. Wu, W. Li, H.S. Qian, Y. Liang, Submicrometer-sized NiO octahedra: facile one-pot solid synthesis, formation mechanism, and chemical conversion into Ni octahedra with excellent microwave-absorbing properties, J. Mater. Chem. 22 (2012) 17494–17504.
[35] S.M. Yoon, W.M. Choi, H. Baik, H.J. Shin, I. Song, M.S. Kwon, J.J. Bae, H. Kim, Y.H. Lee, J.Y. Choi, Synthesis of multilayer graphene balls by carbon segregation from nickel nanoparticles, ACS Nano 6 (2012) 6803–6811.
[36] Q. Chen, Y. Ding, M.W. Chen, Nanoporous metal by dealloying for electrochemical energy conversion and storage, MRS Bull. 43 (2018) 43–48.
[37] L.Q. Lu, J.T.M. De Hosson, Y.T. Pei, Low-temperature synthesis of large-area graphene-based carbon films on Ni, Mater. Des. 144 (2018) 245–255.
[38] L.G. Cancado, A. Jorio, E.H. Martins Ferreira, F. Stavale, C.A. Achete, R.B. Capaz, M.V.O. Moutinho, A. Lombardo, T.S. Kulmala, A.C. Ferrari, Quantifying defects in graphene via Raman spectroscopy at different excitation energies, Nano Lett. 11 (2011) 3190–3196.
[39] D.H. Liu, C. Zhang, G.M. Zhou, W. Lv, G.W. Ling, L.J. Zhi, Q.H. Yang, Catalytic effects in lithium–sulfur batteries: promoted sulfur transformation and reduced shuttle effect, Adv. Sci. 5 (2018), 1700270.
[40] H. Noh, J.C. Song, J.K. Park, H.T. Kim, A new insight on capacity fading of lithium–sulfur batteries: the effect of Li_2S phase structure, J. Power Sources 293 (2015) 329–335.
[41] A.J. Bard, L.R. Faukner, Electrochemical Methods, John Wiley & Sons, New York, 2001, pp. 368–416.
[42] Y. Cui, X.L. Zhao, R.S. Guo, Improved electrochemical performance of $La_{0.7}Sr_{0.3}MnO_3$ and carbon co-coated $LiFePO_4$ synthesized by freeze-drying process, Electrochim. Acta 55 (2010) 922–926.